Nano-Structures & Nano-Objects 12 (2017) 121–129

Contents lists available at ScienceDirect

Nano-Structures & Nano-Objects

journal homepage: www.elsevier.com/locate/nanoso

2,4-dinitrotoluene detected using portable Raman spectrometer and femtosecond laser fabricated Au–Ag nanoparticles and nanostructures

Chandu Byram, Venugopal Rao Soma *

Advanced Centre for Research in High Energy Materials (ACRHEM), University of Hyderabad, Prof. C.R. Rao Road, Hyderabad 500046, India

GRAPHICAL ABSTRACT

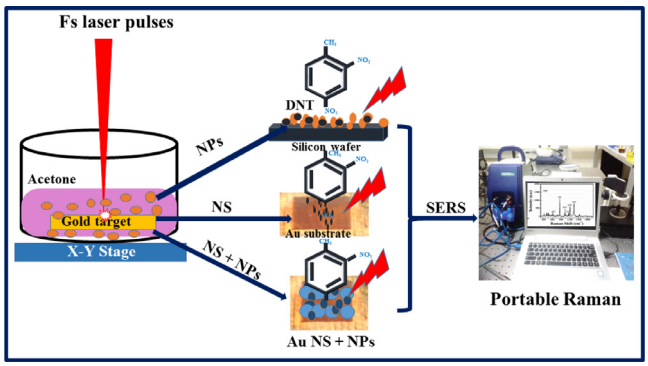

ARTICLE INFO

Article history:
Received 29 July 2017
Received in revised form 7 September 2017
Accepted 29 September 2017

Keywords:
DNT
Nanoparticles
Nanostructures
SERS
Femtosecond laser ablation

ABSTRACT

We report results from our studies on the fabrication of bimetallic nanoparticles (NPs) and nanostructures (NSs) using femtosecond (∼50 fs) laser ablation technique. The NPs and NSs were achieved by immersing bulk targets with different Au–Ag compositions in acetone followed by ablation. We demonstrate their application towards detection of an explosive molecule of 2, 4-Dinitrotoluene, DNT (25 μM) using a portable Raman spectrometer (785 nm). A tuneable surface plasmon peak observed in the UV-Visible absorption spectra with varying Au proportions confirmed the formation of bimetallic NPs. The size, shape and crystallographic phases were investigated by transmission electron microscope (TEM) and selected area diffraction pattern (SAED). The surface morphology of fabricated NSs was characterized using field emission scanning electron microscope (FESEM). Both NPs and NSs were employed as Surface Enhanced Raman Scattering (SERS) substrates for sensing Methylene Blue (MB) and DNT. From the results obtained in this investigation we concluded that $Au_{70}Ag_{30}$ NPs/NSs exhibited superior SERS performance compared to pure Ag, Au and other compositions. A detection limit of $\sim 10^{-9}$ M for MB and $\sim 10^{-6}$ M for DNT was achieved with corresponding enhancement factors of $\sim 10^{7}$ and $\sim 10^{4}$. Furthermore, we have also observed a 'factor of 3' increase in the SERS intensity by simply drop casting Ag NPs on the gaps of $Au_{70}Ag_{30}$ NSs. This clearly demonstrates that individual NPs, NSs and NPs on NSs (hybrid SERS targets) can be achieved in a single experiment and in combination provide efficient means of detecting trace quantities of explosive molecules.

* Corresponding author.
E-mail address: soma_venu@uohyd.ac.in (V.R. Soma).

https://doi.org/10.1016/j.nanoso.2017.09.019
2352-507X/

1. Introduction

During the last decade Surface Enhanced Raman Scattering (SERS) technique has proven to be an efficient analytical tool for recognition of various analyte molecules, owing to its finger print nature, sensitivity and selectivity. SERS has bounteous applications in the fields of explosive detection [1–4], chemical detection [5] and bio-sensing [6,7] etc. Over the last couple of decades, noble metal nanoparticles (NPs)/nanostructures (NSs) with diverse shapes or sizes have been exploited efficaciously as SERS substrates for sensing of variety of molecules due to their strong optical properties in the visible spectral region [7–9]. Gold (Au) and silver (Ag) are widely used as SERS substrates for detection of various molecules. The stability of Ag NPs is inferior compared to Au NPs but Ag NPs provide superior SERS enchantments due to their surface plasmon peaks and near field inter-particle coupling effects. However, Ag NPs are prone to oxidation effects reducing their efficacy. Au NPs are not susceptible to oxidation and, therefore, an approach of combining Ag and Au metals was realized to conglomerate the advantages of Ag with enhanced optical properties and Au with stable chemical properties. The alloy formation of Ag and Au is a viable process with less surface segregation due to similarities between the lattice parameters ($a_{Au} = 4.08$ Å, $a_{Ag} = 4.09$ Å). To fabricate Ag–Au bimetallic NPs, a variety of methods have been proposed during the past years such as co-reduction of metal salts [10] galvanic replacement method [11] and evaporation of bulk alloys [12], which exhibit superior optical [13] and catalytic [14,15] properties compared to monometallic NPs. Xu et al. demonstrated the enhancement in the efficiency of a solar cell by tuning the molar ratio in the composition of Ag-Au alloy NPs when compared to individual NPs [16]. More recently, Chaffin et al [17]. demonstrated theoretically, the electromagnetic enhancements of Ag-Au alloy NPs by considering the Mie theory and the discrete dipole approximation [17]. Many of the chemical methods are sometimes time-consuming, offers lower purity of NPs (presence of surfactants and other toxic chemicals) and needs sophisticated instruments.

Compared to the aforesaid methods, ultrafast laser ablation in liquids (ULAL) is a simple and green technique for simultaneous fabrication of NPs and NSs in a single exposure [18–22]. ULAL offers pure and stable NPs without a necessity of reducing agents or chemicals. In ULAL, a high energy laser pulse interacting with target material immersed in liquid media penetrates the target surface up to a certain depth (nm) followed by the ejection of electrons because of high electric field offered by the laser source. The ejected electrons then oscillate along with the electromagnetic field and collide with atoms of bulk material transferring some of the energy to surrounding lattice. The ablated surface of target heats up suddenly and vaporizes, leading to a plasma formation on a target surface (at the focal point). The generated plasma plume contains atoms, clusters, electrons, ions, etc. The generated plasma plume expands continuously with a creation of shockwave below and above the target surface. As the time progresses, plasma plume cools down and produces cavitation bubble. The cavitation bubble expands up to a maximum radius and then it collapses followed by the generation of NPs [18,20,23]. In one of the earlier studies, Lee et al. demonstrated fabrication of Ag–Au alloy NPs by ablating bulk alloy target in water and they observed a redshift in the plasmon peak with increasing Au proportion [24]. Oscar et al. also synthesized Ag-Au alloy NPs through LAL technique and utilized these NPs for sensing of methylene blue (MB) [25]. Besides these works several composite materials combined with noble metals such as Au–Fe, Ag-graphene etc. were fabricated and utilized for SERS studies [26–31].

In this study, we report results from our efforts on the fabrication of bimetallic nanoparticles (NPs) and nanostructures (NSs) using femtosecond (fs) pulses by ablating the immersed bulk Au–Ag targets in acetone with different Ag/Au compositions. The size, shape and crystallographic phases of the obtained NPs were investigated using TEM and SAED techniques. The surface morphology of the NSs was characterized using FESEM data. The fabricated Ag-Au NPs and NSs were subsequently tested as SERS substrates for sensing a common dye (methylene blue MB, 5 nM) and an explosive molecule (2, 4-dinitrotoluene DNT, 25 μM) using a portable Raman spectrometer (B&W Tek, USA). The goal of our efforts is to achieve uniform enhancement factors for all the common explosive molecules from the in-house prepared SERS targets combined with simple detection methodology of using a portable Raman spectrometer.

2. Experimental details

Bulk Au–Ag targets were prepared by mixing the gold and silver with different weight percentages (Ag, $Au_{20}Ag_{80}$, $Au_{30}Ag_{70}$, $Au_{50}Ag_{50}$, $Au_{70}Ag_{30}$, and $Au_{80}Ag_{20}$, Au). After the preparation, the samples were cleaned thoroughly and cut into small pieces of 1 cm × 1 cm dimensions. The complete experimental procedure was reported in our earlier reports [3,19,32]. Briefly, ablation experiments were performed with a femtosecond amplifier (Ti: sapphire, LIBRA) delivering ∼50 fs pulses with a repetition rate of 1 kHz and at a wavelength of 800 nm. The laser beam pulse energy (∼500 μJ) was focused normally onto the Au–Ag (bulk) target immersed in acetone using a convex lens of 100 mm focal length. The liquid layer height was ∼10 mm above the target surface. The focal point was adjusted by listening to the cracking sound and the plasma formation at the target surface. During the ablation, an *X*–*Y* (ESP 300, Newport, USA) motorized stage was utilized to draw the periodic lines on the substrate with a line spacing of 100 μm and the scanning speeds of 500 μm/s along both directions (*X* and *Y* direction). The ablation time was typically 10 min and each line length was ∼5 mm on the target surface. All the ablation experiments were performed under same conditions such as liquid layer thickness, stage parameters, pulse energy, and time of exposure. Post ablation the colloids were collected and preserved in glass bottles and utilized for characterization and SERS studies. The absorption spectra of colloids were recorded with UV-Visible (PerkinElmer Lambda 750) spectrometer. The shape, size, and crystallinity of the nanoparticles (NPs) were investigated using high-resolution transmission electron microscope (HRTEM, FEI Tecnai G2 S-Twin) and selected area diffraction (SAED) by dropping the tiny drop of colloidal solution on carbon coated copper grid then dried at room temperature. Surface morphology of nanostructures (NSs) was characterized by field emission scanning electron microscope (FESEM, Carl Zeiss). The probe molecules of DNT (dissolved in acetone) and MB (dissolved in methanol) were prepared in stock solution (1×10^{-1} M) and diluted successively to attain the different lower concentrations of (10^{-9} to 10^{-4} M). For the Raman measurements initially nanoparticles (NPs) were dropped on a Silicon substrate and dried. Later 2 ,4-dinitrotoluene (DNT) (25 μM) solution was dropped on NP/NS surface followed by the acquisition of the Raman spectra using portable Raman spectrometer (B&W Tek, USA) with a laser operating at 785 nm wavelength and using an integration time of 5 s.

3. Results and discussions

3.1. UV-visible spectra and characterization

Fig. 1 depicts the normalized UV-visible absorption spectra of Au–Ag colloids obtained in acetone. The surface (SPR) plasmons peaks of obtained Au–Ag NPs were located at 432, 437, 459, 492 and 501 nm for $Au_{20}Ag_{80}$, $Au_{30}Ag_{70}$, $Au_{50}Ag_{50}$, $Au_{70}Ag_{30}$,

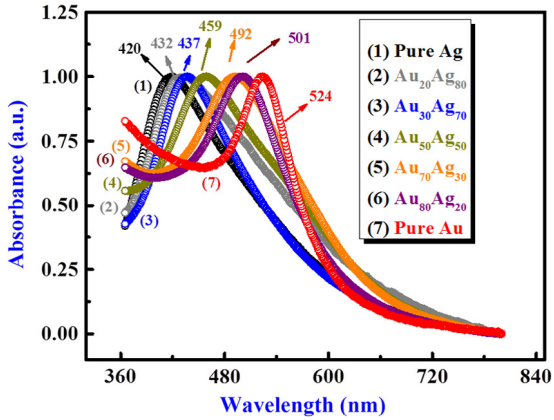

Fig. 1. UV-visible spectra of Au–Ag colloids (1) Ag, (2) $Au_{20}Ag_{80}$, (3) $Au_{30}Ag_{70}$, (4) $Au_{50}Ag_{50}$, (5) $Au_{70}Ag_{30}$, (6) $Au_{80}Ag_{20}$ and (7) Au, obtained in acetone at a pulse energy of 500 μJ.

and $Au_{80}Ag_{20}$ respectively. These peaks are positioned within the SPRs of pure Ag (∼420 nm) and Au (∼524 nm) NPs. From the presented data it was observed the presence of single SPR peak clearly confirmed the formation of bimetallic NPs and possibly there were no core shell formation [24,33]. If there were any core shell NPs present the spectra would have exhibited two SPR peaks. Such peaks were not observed in any of the absorption spectra of the NPs investigated in this work. Moreover, the red shift in the SPR peak was observed with the increase of Au proportion, which is primarily dependent on the material proportion and feebly dependent on the size and shape of the NPs [34,35]. This clearly demonstrates that the SPR peak of Ag-Au NPs can be tuned easily by simply changing the Au proportion, which has a great potential in the fields of solar cells and light trapping, because the scattering efficiency can be tuned in the entire solar spectrum [16].

3.2. TEM characterization studies

The morphological properties and the crystallinity of synthesized NPs were analysed by using high-resolution transmission electron microscope (HRTEM) operating at 200 kV. Fig. 2(a1) and (a2) illustrate the TEM micrographs of fabricated NPs and the corresponding SAED patterns. Well dispersed Ag NPs with spherical shape were observed [Fig. 2(a1)] with insets illustrating their HRTEM images indicating the lattice spacing of 0.24 nm while the corresponding SAED pattern revealed the polycrystalline nature of NPs with Miller planes (1 1 1), (2 0 0) and (2 2 0). Fig. 2(b1) and (b2) depict the TEM image and SAED pattern of $Au_{20}Ag_{80}$ NPs with plane separation of 0.23 nm corresponding to the first ring of Miller plane (1 1 1) and other planes with spacing 0.21 nm (2 0 0) and 0.13 nm (2 2 0). Fig. 2(c1) and (c2) depict the TEM image and SAED pattern of $Au_{30}Ag_{70}$ NPs with lattice plane separation of 0.23 nm [insets of Fig. 2(c1)] and the first, second and third ring in SAED pattern correspond to the miller planes of (1 1 1), (2 0 0), (2 2 0) and (3 1 1). Fig. 2(d1) and (d2) presents the TEM and SAED pattern of $Au_{50}Ag_{50}$ NPs. The measured separation was 0.24 nm corresponding to the first ring of Miller plane (1 1 1) and other planes were (2 0 0), (2 2 0) and (3 1 1) with spacings of 0.198 nm, 0.138 nm, and 0.12 nm. Fig. 3(a1) and (a2), (b1) and (b2), (c1) and (c2) illustrate the TEM and corresponding SAED patterns of $Au_{70}Ag_{30}$, $Au_{80}Ag_{20}$ and Au NPs with measured lattice separations of 0.23 nm, 0.24 nm and 0.238 nm, respectively. The observed plane separations for Au–Ag NPs are compatible with pure Ag and Au phases owing to the structural similarities between Au and Ag, vis-à-vis their lattice constants [$a = 4.08$ Å (Au), $a = 4.09$ Å (Ag)]. The mean size of NPs was calculated by counting >200 particles with software (image J). The obtained mean sizes were ∼10.4 nm, ∼4.8 nm, ∼6.3 nm, ∼4.4 nm, ∼7.3 nm, ∼6.4 nm and ∼8.3 nm for Ag, $Au_{20}Ag_{80}$, $Au_{30}Ag_{70}$, $Au_{50}Ag_{50}$, $Au_{70}Ag_{30}$, $Au_{80}Ag_{20}$, and Au NPs, respectively. [The data is presented in figure S1 of supporting information (S.I.).]

The difference in mean sizes was observed for different compositions though the ablation experiments were performed at similar conditions. This could probably be due to the variation of ablation threshold of the alloys as compared to the pure Au and Ag targets [3,36]. This could also have resulted in the variation of ablation yield with different targets (alloys versus pure metals). In earlier reports, Manjón et al. observed the lower ablation mass for Ag as compared to Au–Ag target which could affect the variation of mean sizes [36].

The mechanism involved in the formation NPs can be explained briefly as follows. When the short laser pulse interacts with the target, high-temperature plasma is generated through absorption of the input laser energy and, consequently, atoms from the target surface are ejected through vaporization, followed by the formation of dense atoms (Ag and Au) near the laser spot. Lee et al. from their nanosecond ablation studies clearly suggested that the generated bimetallic/alloy NPs from the bulk Ag-Au targets were neither a simple mixture of individual metals (Au and Ag) nor the core shell particles [24]. Recent report on the nanosecond ablation of the Ag/Au alloys clearly established that the fact that Ag, Au atoms were randomly distributed all through the fabricated NPs and that no preferential sites for these NPs were detected [25]. The observed bimetallic NPs mean sizes and separations in the present case were in intermediate range of the sizes of monometallic NPs [37]. This could be attributed to the miscibility nature of Ag and Au at any proportion in bulk or nanometre scale due to their almost identical lattice parameters [13]. The main difficulty in LAL is the size control and homogeneity of NPs because the particles ejected from the target surface will interact with subsequent laser pulse resulting in further size reduction through fragmentation of the produced NPs. Therefore, deeper understanding is needed for precise size control of NPs when they are interacting with laser beams.

3.3. FESEM characterization studies

Fig. 4 illustrates FESEM images of the femtosecond fabricated Ag, Au and Au-Ag NSs in acetone with pulse energy of 500 μJ, namely (a) Ag (b) $Au_{20}Ag_{80}$ (c) $Au_{30}Ag_{70}$ (d) $Au_{50}Ag_{50}$ (e) $Au_{70}Ag_{30}$ (f) $Au_{80}Ag_{20}$ (g) Au NSs while their insets show the low magnification images. In the case of Ag NS [Fig. 4(a)], nanocavities surrounded by nanorims with the diameter ranging from 30 to 70 nm were observed. As shown in Fig. 4(b) $Au_{20}Ag_{80}$ NSs were covered with highly dense nano-protrusions and similarly $Au_{30}Ag_{70}$ NSs [Fig. 4(c)] consisted of nano-protrusions covered with nanocavities of few ∼nm size. Fig. 4(d) clearly shows spherical NPs of diameter ∼20 nm formed on top of the $Au_{50}Ag_{50}$ NSs. Fig. 4(e) depicts the cylindrical NPs (length ∼100 nm, width ∼55 nm) deposited on to the $Au_{70}Ag_{30}$ NSs. Fig. 4(f) illustrates nanoparticle grains with arbitrary shapes and periodicity of ∼25 nm on top of the $Au_{80}Ag_{20}$ NSs. Finally Fig. 4(g) shows nanopores along with nanoprotrusions (∼20 nm diameter) being formed on top of the Au NS. In the present study, the nanoscale features of few nm were observed on the substrates with femtosecond pulses. The morphology of NSs consisting of nanopores/nanorims of irregular shapes accompanied by nanoprotrusions can be attributed to the (i) spallation of cavitation bubble at target liquid interface (ii) ablated nanoparticle fusion and re-deposition on to the irradiated position of the target [38,39]. The formation of NSs on the metallic target surface in liquid media during femtosecond pulse ablation is a complex phenomenon and involves several complicated stages. When an

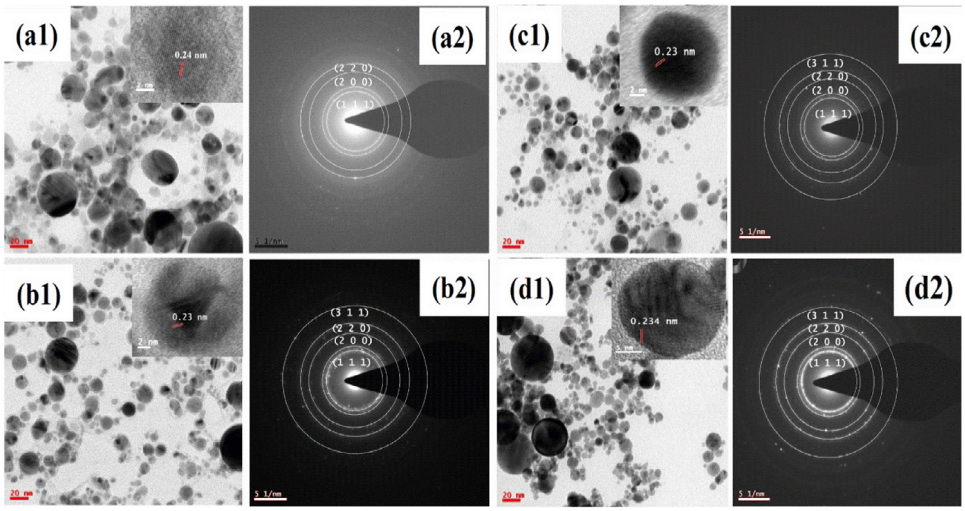

Fig. 2. TEM images of NPs insets show their HRTEM image (a1 and a2) Ag NPs and corresponding SAED pattern, (b1 and b2) $Au_{20}Ag_{80}$ NPs and corresponding SAED pattern, (c1 and c2) $Au_{30}Ag_{70}$ NPs and corresponding SAED pattern, (d1 and d2) $Au_{50}Ag_{50}$ NPs and corresponding SAED pattern, respectively.

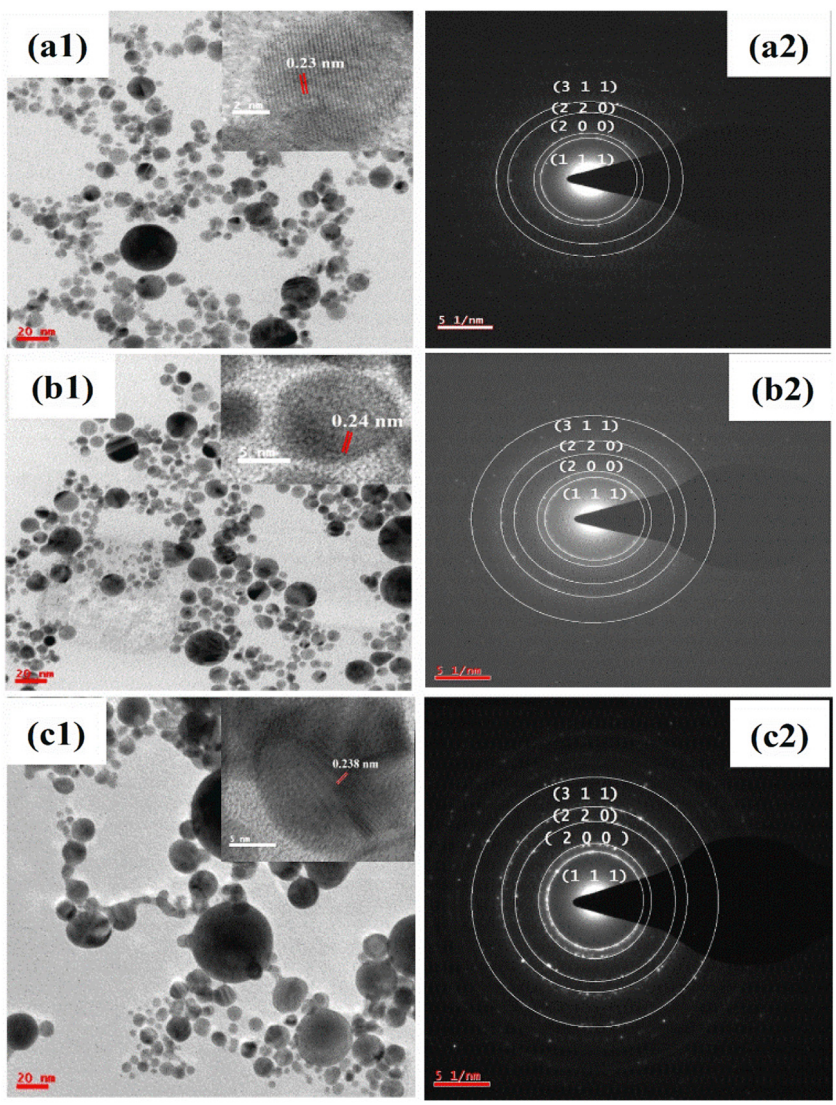

Fig. 3. TEM images of NPs insets show their HRTEM image (a1 and a2) $Au_{70}Ag_{30}$ and corresponding SAED pattern, (b1 and b2) $Au_{80}Ag_{20}$ NPs and corresponding SAED pattern, (c1 and c2) Au NPs and corresponding SAED pattern, respectively.

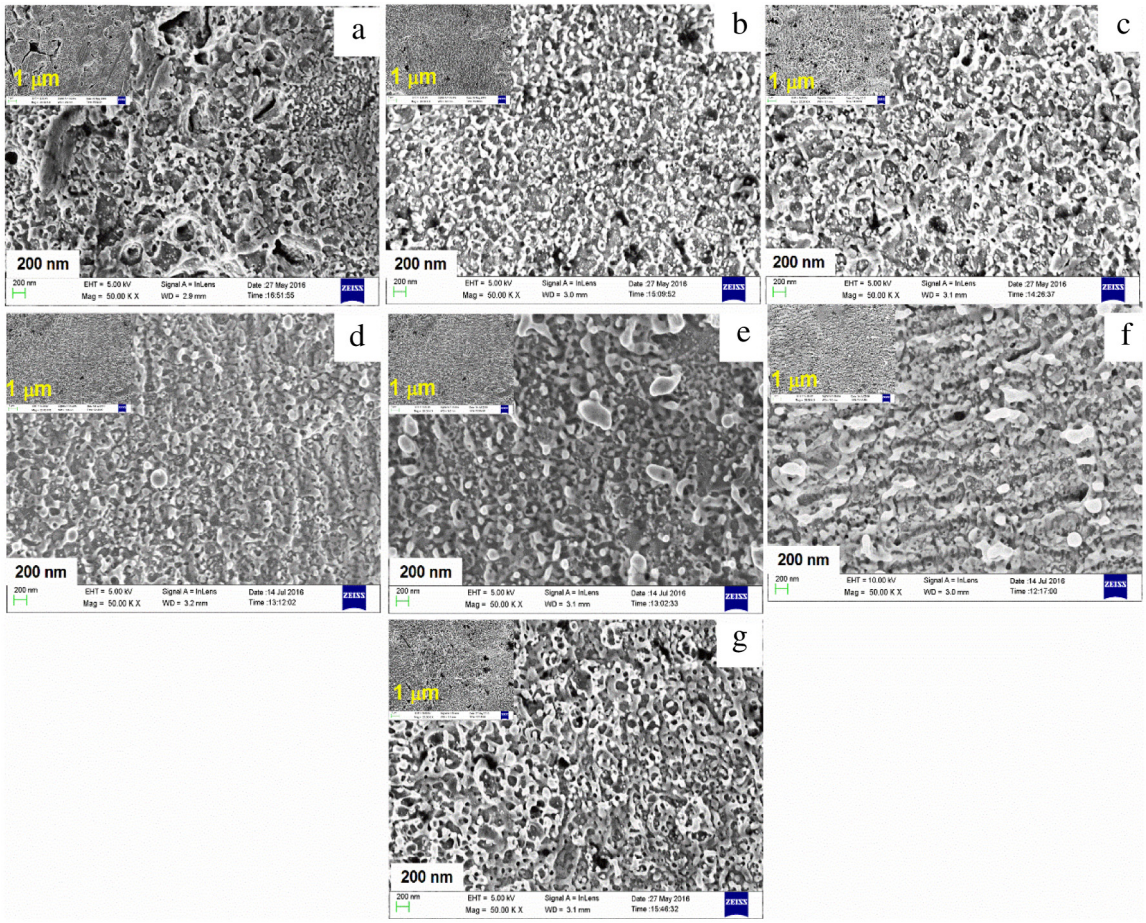

Fig. 4. FESEM images of laser machined portions on Au–Ag targets (a) Ag, (b) $Au_{20}Ag_{80}$, (c) $Au_{30}Ag_{70}$, (d) $Au_{50}Ag_{50}$, (e) $Au_{70}Ag_{30}$, (f) $Au_{80}Ag_{20}$, (g) Au NSs and insets show their low magnification images.

ultrafast pulse interacts with the target material surface melting takes place at room temperature. As a result, liquid vaporizes and the higher pressure was induced at the target surface, which results in nano-texturing on the solid surface. The nano-texturing could result when the pulse duration is <1 ns [40,41]. The diverse morphology of NSs can induce giant local electric fields through the propagating surface plasmons on illumination of the laser at the suitable wavelength. This kind of NSs plays substantial role in enhancing the Raman signal of the analyte molecule when the molecule is near the NS surface through the SERS phenomenon.

3.4. SERS studies using both Au–Ag NPs and NSs

The SERS performance of obtained bimetallic NPs was tested with probe molecules such as MB (50 nM) and DNT (25 μM). Initially, 10 μL of Au–Ag NPs were dropped on individual silicon wafers and dried, later 10 μL of dye/explosive molecule were dropped over the NPs film and acquired the SERS signal by utilizing portable Raman spectrometer of 785 nm wavelength. Fig. 5(a) depicts the SERS spectra of MB (50 nM) obtained on various compositions of bimetallic NP films (NPs drop-casted on Si). For MB [data presented in Fig. 3(a)], the characteristic Raman modes observed at 449 cm^{-1}, 589 cm^{-1} are assigned to the C–N–C skeletal deformation while the 1396 cm^{-1}, 1621 cm^{-1} modes correspond to the C–N symmetric stretching and C–C ring stretching, which are consistent with the earlier reports [42]. The normal Raman spectra of MB and DNT (powder) are presented in Fig. S3 (S.I.). The performance of NPs/NSs were evaluated by calculating the enhancement factor (EF) using following formula (1) [43].

$$EF = \frac{I_{SERS}}{I_{RAMAN}} \frac{C_{HC}}{C_{LC}} \quad (1)$$

Where I_{SERS} is the integrated intensity of is highly elevated Raman bond of analyte molecule under consideration from the NP/NS surface, and I_{RAMAN} is the integrated intensity of the same band obtained on a silicon substrate. C_{HC} is the high concentration of analyte molecule generating the normal Raman intensity from the silicon substrate, and C_{LC} is the low concentration of analyte molecule generating the Raman intensity from the nanostructured substrate. The EFs for Au–Ag NPs were estimated by comparing the prominent mode of MB (1621 cm^{-1}) observed from the SERS spectra with normal spectra of the same mode observed from Si target. The estimated EFs are 2.7×10^6, 1.1×10^6, 1.83×10^6, 9.9×10^5, 3.2×10^6, 1.34×10^6 and 1.67×10^6 for Ag, $Au_{20}Ag_{80}$, $Au_{30}Ag_{70}$, $Au_{50}Ag_{50}$, $Au_{70}Ag_{30}$, and $Au_{80}Ag_{20}$ and Au NP films, respectively (complete EFs are summarized in table S1, S.I.).

From the presented data, $Au_{70}Ag_{30}$NPs film exhibited superior SERS enhancements compared to the other combinations including monometallic Ag and Au NPs. Polavarapu et al. reported the detection of malachite green (10^{-9} M), R6G (10^{-12}M), and thiabendazole (20 ppm) using pen on paper approach with Ag NPs, Au NRs and Au NPs using a micro-Raman spectrometer operated at 532, 632 and 785 nm wavelengths and achieved enhancement factors $\sim10^5$ [44–46]. In our case, we could detect MB at $\sim10^{-8}$ M and DNT at 10^{-6}M concentrations (4.55 ppm) with NPs using portable Raman spectrometer with EFs of 10^6 and 10^4, which is comparable to with their studies. Further, in the former case [44–46] they employed a bulk micro-Raman spectrometer where the

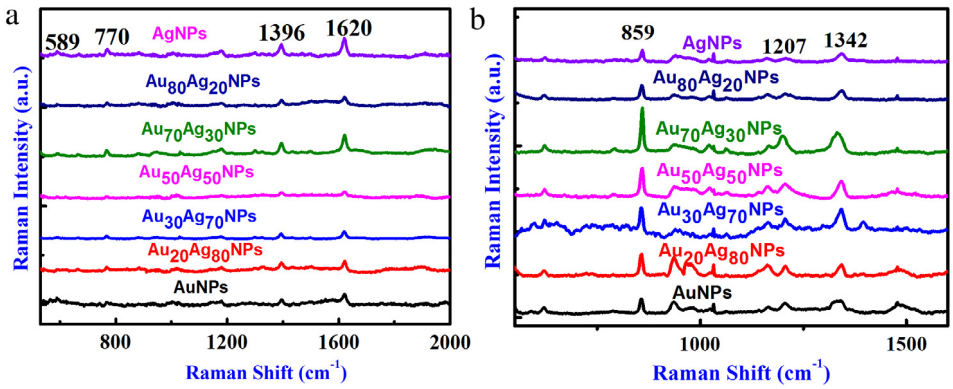

Fig. 5. SERS spectra of (a) MB (50 nM) (b) DNT (25 μM) recorded from Ag, $Au_{20}Ag_{80}$, $Au_{30}Ag_{70}$, $Au_{50}Ag_{50}$, $Au_{70}Ag_{30}$, and $Au_{80}Ag_{20}$ and Au NPs (NPs drop casted on Si), respectively.

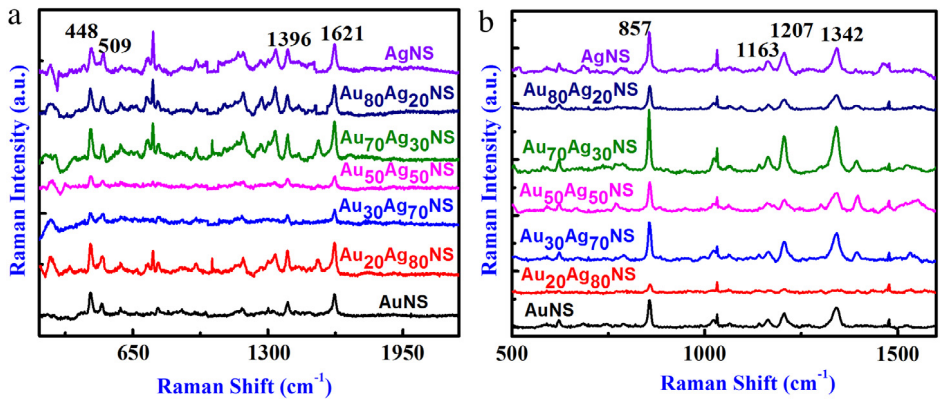

Fig. 6. SERS spectra of (a) MB (5 nM) (b) DNT (25 μM) recorded from Ag, $Au_{20}Ag_{80}$, $Au_{30}Ag_{70}$, $Au_{50}Ag_{50}$, $Au_{70}Ag_{30}$, and $Au_{80}Ag_{20}$ and Au NSs, respectively.

measurements involved are complicated and not easy to transport the Raman system (for example, to the outdoors) whereas our measurements were performed with a portable Raman system (4–5 kgs) and is easily portable and will find practical applications. Similarly, the SERS measurements were also performed for an explosive molecule of DNT. Fig. 5(b) depicts the SERS spectra of DNT (25 μM) obtained on Au–Ag NP films. The prominent modes of DNT [depicted in Fig. 5(b)] were observed at 857, 1163, 1207 and 1342 cm^{-1}, which are attributed to the NO_2 out-of-plane mode, methyl H–C–H asymmetric bend, H–C–C in plane bending and NO_2 symmetric stretching, respectively [vibrational assignments are presented in table S2 of S.I.]. The observed modes for DNT are consistent with previous reports [47,48]. The EFs were estimated by considering the strong Raman mode of DNT (857 cm^{-1}) are 8.8×10^3, 1.84×10^3, 8.31×10^3, 6.14×10^3, 1.35×10^4, 4.99×10^3 and 5.87×10^3 for Ag, $Au_{20}Ag_{80}$, $Au_{30}Ag_{70}$, $Au_{50}Ag_{50}$, $Au_{70}Ag_{30}$, and $Au_{80}Ag_{20}$ and Au NP films, respectively. Earlier reports have demonstrated the detection of DNT up to $\sim10^{-11}$ M using various NPs with diverse shapes using micro-Raman spectrometers (532 nm, 632 nm) [49,50]. However, those NPs were fabricated using chemical methods by adding reducing agents and required multiple stages for fabrication. In the present case, we have detected $\sim10^{-6}$ M DNT with a portable Raman spectrometer by using NPs/NSs fabricated in a single experiment. The considerable number of counts observed even for the lowest concentration detected clearly suggests that at least one more order of magnitude lower concentration can easily be detected with the present set up. Further, by increasing the density of NPs on the substrates (either on Silicon or the metal NS itself), which can be easily achieved by drop casting multiple numbers of NPs colloidal drops, we can expect additional improvements in the EF's because of creation of higher number of hotspots. However, these studies need to be performed systematically and clear data should be obtained before concluding about the improvements. The sizes/shapes of NPs will play a crucial role in the variation of SERS intensities. For example, Kumari et al. demonstrated the effect of Ag NPs size from 20 to 100 nm with silica shell thickness of ∼2 nm on the SERS intensity [51]. They have observed no SERS signal when the silica shell thickness was 2 nm on smaller size Ag NPs while for larger particles it was observed. There could be multiple reasons for variation in SERS intensity not only the size of NPs but also effect of plasmon peaks, distance between the analyte and nanoparticles surfaces. If the distance between the NPs is <1 nm there could be higher possibility to achieve superior SERS intensities. In the present study, observed NPs mean sizes in between ∼4 and 10 nm. One needs to obtain bigger nanoparticles through laser ablation studies (optimization is required in terms of energy, scanning speed, liquid levels etc.) and then using fragmentation method to obtain smaller sized NPs and only then it will be then possible to perform size dependent studies.

The fabricated Au–Ag NSs were also tested with analytes of MB (5 nM) and DNT (25 μM). Fig. 6(a) depicts the SERS spectra of MB (5 nM) recorded on bimetallic NSs in including pure Ag and Au substrates. The predicted EFs are 2×10^7, 2.3×10^7, 1×10^7, 8.9×10^6, 3×10^7, 2.1×10^7 and 1.6×10^7 for Ag, $Au_{20}Ag_{80}$, $Au_{30}Ag_{70}$, $Au_{50}Ag_{50}$, $Au_{70}Ag_{30}$, $Au_{80}Ag_{20}$ and Au NSs, respectively. Compared to all combinations including pure Ag and Au NSs, $Au_{70}Ag_{30}$NSs exhibited superior SERS enhancement. To evaluate the sensitivity of $Au_{70}Ag_{30}$ NS, a systematic study was employed by recording the

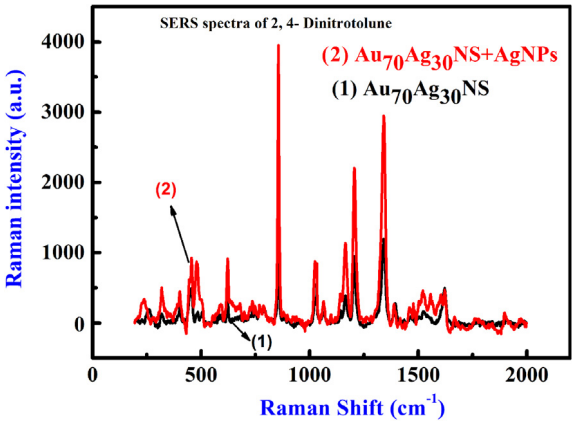

Fig. 7. SERS spectra of 2, 4-dinitrotoluene (25 μM) recorded on (1) $Au_{70}Ag_{30}$ NS (black one) (2) $Au_{70}Ag_{30}$ NS+AgNPs (red one) using portable Raman spectrometer with 785 nm excitation.

SERS spectra of MB ranging from 10^{-6} to 10^{-9} M. The concentration of MB decreased monotonically with the SERS intensity, even at the low concentration of 10^{-9} M, the major Raman modes of MB were clearly visible (data shown in Fig. S2 of S.I). The observed EFs in the present case are comparable with earlier reports. The prior-mentioned substrates were reused the second time for the identification of an explosive molecule (2, 4-dinitrotolune) after nominal cleaning with acetone and deionized water in the ultrasonic bath for 20 min. Before conducting the SERS measurements of DNT, Raman signals were acquired on the cleaned substrates and we did not observe any modes of MB on the Au–Ag NSs. Later SERS signals were acquired for DNT (25 μM) on the Au–Ag NSs and the data is shown in Fig. 6(b). In the case of DNT, the evaluated EFs were 5.58×10^3, 1×10^4, 1.13×10^4, 1.33×10^4, 2.17×10^4, 6.7×10^3 and 6.6×10^3 for Ag, $Au_{20}Ag_{80}$, $Au_{30}Ag_{70}$, $Au_{50}Ag_{50}$, $Au_{70}Ag_{30}$, $Au_{80}Ag_{20}$ and Au NSs, respectively. Similarly, we could achieved the greater SERS enhancement for the $Au_{70}Ag_{30}$ NS.

Fig. 7 depicts the SERS spectra of DNT recorded on (1) $Au_{70}Ag_{30}$NS (black line) and (2) enhanced SERS spectra in the presence of Ag NPs on $Au_{70}Ag_{30}$ NS (red line). An enhancement of ∼3 times in SERS intensity was achieved when the NPs are drop casted on the nanostructured surface. In both the cases of (i) NPs, (ii) NSs as a SERS platform for the detection of MB and DNT, the $Au_{70}Ag_{30}$NSs combination provided superior enhancements in the SERS intensity compared to the other combinations including pure Au and Ag NSs and NPs. Probably, the hybridization in the $Au_{70}Ag_{30}$ sample was superior to other combinations, and consequently, greater SERS enchantments were observed for this combination. Fan et al. [52] demonstrated that the SERS enhancement also depends on analyte stability and as well as the Au–Ag proportions. From the FESEM image data of Fig. 4(e) we can conclude that $Au_{70}Ag_{30}$ displayed more number of NPs with arbitrary shapes on top of the NSs compared to other combinations, which could also be the plausible reason for the observed EFs for this combination. To this extent, we also tested the enhancement of SERS intensity by drop casting Ag NPs (collected separately in the earlier ablation experiments) in the gaps of $Au_{70}Ag_{30}$ NS and we could observe a clear ∼3 times enhancement in the SERS intensity (data presented in Fig. 7). Recently, few studies have been demonstrated that, when the NPs reside on the nano-textured surface they produce higher SERS enhancements by generating higher number of hot spots [53,54].

It is noteworthy to mention here that we achieved the different EFs of $\sim10^7$, $\sim10^4$ for MB and DNT, which could be ascribed to (i) absorption peak of the MB (∼650 nm) molecule close to the excitation wavelength [55,56] than the DNT absorption peak (∼250 nm) (ii) the chemical stability of analyte when it is located close to the NP/NS surface [52] (iii) morphology of NPs or NSs which is crucial factor for generating higher number of hotspots [7,57], which leads to the observation of superior SERS enchantment factors. Our group had earlier reported SERS studies of explosive molecules of FOX-7 and 1-NPZ (1-Nitropyrazole) using Ag–Au NPs in three different molar ratios [3]. Those NSs and NPs were achieved with different writing conditions (scanning speeds and different stages were used) and different input energies. The higher EFs obtained in that case could be due to the different fabrication conditions resulting in diverse surface morphologies in the case of NSs and varied sizes/distributions in the case of NPs. Moreover, the usage of 532 nm Raman excitation source in that case (whereas 785 nm is used in the present study), which is near to the absorption wavelength of Ag-Au NPs, could have reinforced the observed EFs. Our pursuit over the last few years has been to achieve robust SERS targets that provide uniform EF's for the most common explosive molecules. This study provides a small step towards achieving that goal. The exact proportion of Ag-Au combination for achieving larger SERS enchantment is not clearly understood so far owing to the profound effects of NPs shape/ NSs morphology and excitation wavelength, which mandates further detailed investigations.

4. Summary

We have successfully demonstrated the fabrication of a variety of Au–Ag NPs and NSs for SERS based detection of an explosive molecule. These were obtained by ablating the bulk Au–Ag targets (with different weight percentages of Au and Ag) in liquid using femtosecond laser pulses in a single experiment. The SPR peaks were observed in the 420–524 nm spectral range for Au–Ag NPs and were achieved by changing the Au proportion. The fabricated NSs and NPs were used to detect $\sim10^{-9}$ M MB dye and $\sim10^{-6}$ M DNT, with the corresponding enhancement factors of $\sim10^7$ and $\sim10^4$, respectively. From the data obtained in this study we concluded that $Au_{70}Ag_{30}$ composition provided superior SERS enhancements for the dye MB (5 nM) and explosive molecules DNT (25 μM) when compared to other combinations including monometallic NPs and NSs.

Acknowledgements

Venugopal Rao Soma thanks DRDO, India for financial support through the project sanction #ERIP/ER/1501138/M/01/319/D(R&D) dated 27.02.2017. We also thank the anonymous reviewers for their valuable suggestions.

Appendix A. Supplementary data

Supplementary material related to this article can be found online at https://doi.org/10.1016/j.nanoso.2017.09.019.

References

[1] A. Chou, E. Jaatinen, R. Buividas, G. Seniutinas, S. Juodkazis, E.L. Izake, P.M. Fredericks, SERS substrate for detection of explosives, Nanoscale 4 (23) (2012) 7419.

[2] S. Hamad, G.K. Podagatlapalli, M.A. Mohiddon, V.R. Soma, Cost effective nanostructured copper substrates prepared with ultrafast laser pulses for explosives detection using surface enhanced Raman scattering, Appl. Phys. Lett. 104 (26) (2014) 263104.

[3] G.K. Podagatlapalli, S. Hamad, S.V. Rao, Trace-level detection of secondary explosives using hybrid silver–gold nanoparticles and nanostructures achieved with femtosecond laser ablation, J. Phys. Chem. C 119 (29) (2015) 16972.

[4] C. Byram, S.S.B. Moram, A.K. Shaik, V.R. Soma, Versatile gold based SERS substrates fabricated by ultrafast laser ablation for sensing picric acid and ammonium nitrate, Chem. Phys. Lett. 685 (2017) 103.
[5] Y. Li, J. Dykes, N. Chopra, Silicon nanowire-gold nanoparticle heterostructures for surface-enhanced Raman spectroscopy, Nano-Struct. Nano-Obj. 7 (2016) 12.
[6] B. Sharma, R.R. Frontiera, A.-I. Henry, E. Ringe, R.P. Van Duyne, SERS: Materials, applications, and the future, Mater. Today 15 (1) (2012) 16.
[7] H. Ko, S. Singamaneni, V.V. Tsukruk, Nanostructured surfaces and assemblies as SERS media, Small 4 (10) (2008) 1576.
[8] L. Polavarapu, L.M. Liz-Marzán, Towards low-cost flexible substrates for nanoplasmonic sensing, Phys. Chem. Chem. Phys. 15 (15) (2013) 5288.
[9] C.H. Lee, M.E. Hankus, L. Tian, P.M. Pellegrino, S. Singamaneni, Highly sensitive surface enhanced raman scattering substrates based on filter paper loaded with plasmonic nanostructures, Anal. Chem. 83 (23) (2011) 8953.
[10] I. Srnová-Šloufová, B. Vlčková, Z. Bastl, T.L. Hasslett, Bimetallic (Ag) Au nanoparticles prepared by the seed growth method: Two-dimensional assembling, characterization by energy dispersive X-ray analysis, X-ray photoelectron spectroscopy, and surface enhanced Raman spectroscopy, and proposed mechanism of growth, Langmuir 20 (8) (2004) 3407.
[11] Q. Zhang, J.Y. Lee, J. Yang, C. Boothroyd, J. Zhang, Size and composition tunable Ag–Au alloy nanoparticles by replacement reactions, Nanotechnology 18 (24) (2007) 245605.
[12] M.Y. Khaywah, S. Jradi, G. Louarn, Y. Lacroute, J. Toufaily, T. Hamieh, P.-M. Adam, Ultrastable, uniform, reproducible, and highly sensitive bimetallic nanoparticles as reliable large scale sers substrates, J. Phys. Chem. C 119 (46) (2015) 26091.
[13] R. Intartaglia, G. Das, K. Bagga, A. Gopalakrishnan, A. Genovese, M. Povia, E. Di Fabrizio, R. Cingolani, A. Diaspro, F. Brandi, Laser synthesis of ligand-free bimetallic nanoparticles for plasmonic applications, Phys. Chem. Chem. Phys. 15 (9) (2013) 3075.
[14] A.-Q. Wang, J.-H. Liu, S. Lin, T.-S. Lin, C.-Y. Mou, A novel efficient Au–Ag alloy catalyst system: preparation, activity, and characterization, J. Catal. 233 (1) (2005) 186.
[15] A.-Q. Wang, C.-M. Chang, C.-Y. Mou, Evolution of catalytic activity of Au—Ag bimetallic nanoparticles on mesoporous support for CO oxidation, J. Phys. Chem. B 109 (40) (2005) 18860.
[16] M. Xu, J. Feng, Y.-S. Liu, Y. Jin, H.-Y. Wang, H.-B. Sun, Effective and tunable light trapping in bulk heterojunction organic solar cells by employing Au-Ag alloy nanoparticles, Appl. Phys. Lett. 105 (15) (2014) 153303.
[17] E. Chaffin, R.T. O'Connor, J. Barr, X. Huang, Y. Wang, Dependence of SERS enhancement on the chemical composition and structure of Ag/Au hybrid nanoparticles, J. Chem. Phys. 145 (5) (2016) 054706.
[18] G. Krishna Podagatlapalli, S. Hamad, S.P. Tewari, S. Sreedhar, M.D. Prasad, S. Venugopal Rao, Silver nano-entities through ultrafast double ablation in aqueous media for surface enhanced Raman scattering and photonics applications, J. Appl. Phys. 113 (7) (2013) 073106.
[19] G.K. Podagatlapalli, S. Hamad, M.A. Mohiddon, S.V. Rao, Fabrication of nanoparticles and nanostructures using ultrafast laser ablation of silver with bessel beams, Laser Phys. Lett. 12 (3) (2015) 036003.
[20] D. Zhang, B. Gökce, S. Barcikowski, Laser synthesis and processing of colloids: Fundamentals and applications, Chem. Rev. 117 (5) (2017) 3990.
[21] A. Kumar, M. Prasad, S. Shail, C. Baghra, B. Mohanty, R. Bhatt, P. Behere, M. Afzal, A. Kumar, S. Neogy, Synthesis of uranium-di-oxide nanoparticles by pulsed laser ablation in ethanol and their characterisation, Nano-Struct. Nano-Obj. 7 (2016) 75.
[22] K.M. Tibbetts, J. Odhner, S. Vaddypally, B. Tangeysh, E.B. Cerkez, D.R. Strongin, M.J. Zdilla, R.J. Levis, Amorphous aluminum-carbide and aluminum–magnesium-carbide nanoparticles from gas phase activation of trimethylaluminum and octamethyldialuminummagnesium using simultaneous spatially and temporally focused ultrashort laser pulses, Nano-Struct. Nano-Obj. 6 (2016) 1.
[23] V. Amendola, M. Meneghetti, Laser ablation synthesis in solution and size manipulation of noble metal nanoparticles, Phys. Chem. Chem. Phys. 11 (20) (2009) 3805.
[24] I. Lee, S.W. Han, K. Kim, Production of Au–Ag alloy nanoparticles by laser ablation of bulk alloys, Chem. Commun. (18) (2001) 1782.
[25] O. Olea-Mejía, M. Fernández-Mondragón, G. Rodríguez-de la Concha, M. Camacho-López, SERS-active Ag, Au and Ag–Au alloy nanoparticles obtained by laser ablation in liquids for sensing methylene blue, Appl. Surf. Sci. 348 (2015) 66.
[26] F. Bertorelle, M. Ceccarello, M. Pinto, G. Fracasso, D. Badocco, V. Amendola, P. Pastore, M. Colombatti, M. Meneghetti, Efficient AuFeOx nanoclusters of laser-ablated nanoparticles in water for cells guiding and surface-enhanced resonance raman scattering imaging, J. Phys. Chem. C 118 (26) (2014) 14534.
[27] H. He, H. Wang, K. Li, J. Zhu, J. Liu, X. Meng, X. Shen, X. Zeng, W. Cai, Green and tunable decoration of graphene with spherical nanoparticles based on laser ablation in water: A case of ag nanoparticle/graphene oxide sheet composites, Langmuir 32 (7) (2016) 1667.
[28] W. Xu, J. Xiao, Y. Chen, Y. Chen, X. Ling, J. Zhang, Graphene-veiled gold substrate for surface-enhanced Raman spectroscopy, Adv. Mater. 25 (6) (2013) 928.
[29] J.E. Weis, J. Vejpravova, T. Verhagen, Z. Melnikova, S. Costa, M. Kalbac, Surface-enhanced Raman spectra on graphene, J. Raman Spectrosc. (2017). http://dx.doi.org/10.1002/jrs.5228. in press.
[30] Z. Chen, L. Qiu, Y. Tian, Y.-I. Lee, X. Hou, L. Wu, Surface-enhanced Raman scattering using monolayer graphene-encapsulated Ag nanoparticles as a substrate for sensitive detection of 2, 4, 6-trinitrotoluene, Anal. Methods 9 (21) (2017) 3105.
[31] J. Yu, Y. Ma, C. Yang, H. Zhang, L. Liu, J. Su, Y. Gao, SERS-active composite based on rGO and Au/Ag core–shell nanorods for analytical applications, Sensors Actuators B 254 (2018) 182.
[32] S. Venugopal Rao, G.K. Podagatlapalli, S. Hamad, Ultrafast laser ablation in liquids for nanomaterials and applications, J. Nanosci. Nanotechnol. 14 (2) (2014) 1364.
[33] Y.-H. Chen, C.-S. Yeh, A new approach for the formation of alloy nanoparticles: laser synthesis of gold–silver alloy from gold–silver colloidal mixturesElectronic supplementary information (ESI) available: Experimental details, UV–VIS spectra, TEM images and EDX analysis for molar ratios (Au: Ag) of 1: 2 and 2: 1, Chem. Commun. (4) (2001) 371 See http://www.rsc.org/suppdata/cc/b0/b009854j.
[34] S. Link, Z.L. Wang, M. El-Sayed, Alloy formation of gold— silver nanoparticles and the dependence of the plasmon absorption on their composition, J. Phys. Chem. B 103 (18) (1999) 3529.
[35] G.C. Papavassiliou, Surface plasmons in small Au-Ag alloy particles, J. Phys. F: Met. Phys. 6 (4) (1976) L103.
[36] A. Menéndez-Manjón, A. Schwenke, T. Steinke, M. Meyer, U. Giese, P. Wagener, S. Barcikowski, Ligand-free gold–silver nanoparticle alloy polymer composites generated by picosecond laser ablation in liquid monomer, Appl. Phys. A 110 (2) (2013) 343.
[37] M. Vinod, K. Gopchandran, Au, Ag and Au: Ag colloidal nanoparticles synthesized by pulsed laser ablation as SERS substrates, Prog. Nat. Sci. 24 (6) (2014) 569.
[38] A.Y. Vorobyev, C. Guo, Direct femtosecond laser surface nano/microstructuring and its applications, Laser Photon. Rev. 7 (3) (2013) 385.
[39] A. Vorobyev, C. Guo, Multifunctional surfaces produced by femtosecond laser pulses, J. Appl. Phys. 117 (3) (2015) 033103.
[40] E.V. Barmina, M. Barberoglu, V. Zorba, A.V. Simakin, E. Stratakis, K. Fotakis, G.A. Shafeev, Surface nanotexturing of tantalum by laser ablation in water, Quantum Electron. 39 (1) (2009) 89.
[41] E.V. Barmina, E. Stratakis, K. Fotakis, G.A. Shafeev, Generation of nanostructures on metals by laser ablation in liquids: New results, Quantum Electron. 40 (11) (2010) 1012.
[42] G.-N. Xiao, S.-Q. Man, Surface-enhanced raman scattering of methylene blue adsorbed on cap-shaped silver nanoparticles, Chem. Phys. Lett. 447 (4) (2007) 305.
[43] E. Le Ru, E. Blackie, M. Meyer, P.G. Etchegoin, Surface enhanced Raman scattering enhancement factors: A comprehensive study, J. Phys. Chem. C 111 (37) (2007) 13794.
[44] L. Polavarapu, A.L. Porta, S.M. Novikov, M. Coronado-Puchau, L.M. Liz-Marzán, Pen-on-paper approach toward the design of universal surface enhanced raman scattering substrates, Small 10 (15) (2014) 3065.
[45] S. Gómez-Graña, C. Fernández-López, L. Polavarapu, J.-B. Salmon, J. Leng, I. Pastoriza-Santos, J. Pérez-Juste, Gold nanooctahedra with tunable size and microfluidic-induced 3D assembly for highly uniform SERS-active supercrystals, Chem. Mater. 27 (24) (2015) 8310.
[46] C. Fernández-López, L. Polavarapu, D.M. Solís, J.M. Taboada, F. Obelleiro, R. Contreras-Cáceres, I. Pastoriza-Santos, J. Pérez-Juste, Gold nanorod–pnipam hybrids with reversible plasmon coupling: Synthesis, modeling, and sers properties, ACS Appl. Mater. Interfaces 7 (23) (2015) 12530.
[47] P.M. Fierro-Mercado, S.P. Hernández-Rivera, Highly sensitive filter paper substrate for sers trace explosives detection, Int. J. Spectrosc. 2012 (2012).
[48] J. Lee, B. Hua, S. Park, M. Ha, Y. Lee, Z. Fan, H. Ko, Tailoring surface plasmons of high-density gold nanostar assemblies on metal films for surface-enhanced Raman spectroscopy, Nanoscale 6 (1) (2014) 616.
[49] J.Y. Xu, J. Wang, L.T. Kong, G.C. Zheng, Z. Guo, J.H. Liu, SERS detection of explosive agent by macrocyclic compound functionalized triangular gold nanoprisms, J. Raman Spectrosc. 42 (9) (2011) 1728.
[50] P. Sajanlal, T. Pradeep, Functional hybrid nickel nanostructures as recyclable SERS substrates: Detection of explosives and biowarfare agents, Nanoscale 4 (11) (2012) 3427.

[51] G. Kumari, J. Kandula, C. Narayana, How far can we probe by SERS? J. Phys. Chem. C 119 (34) (2015) 20057.
[52] M. Fan, F.-J. Lai, H.-L. Chou, W.-T. Lu, B.-J. Hwang, A.G. Brolo, Surface-enhanced Raman scattering (SERS) from Au: Ag bimetallic nanoparticles: The effect of the molecular probe, Chem. Sci. 4 (1) (2013) 509.
[53] Z.M. Jin, W. Gu, X.B. Shi, Z.K. Wang, Z.Q. Jiang, L.S. Liao, A novel route to surface-enhanced Raman scattering: Ag nanoparticles embedded in the nanogaps of a Ag substrate, Adv. Opt. Mater. 2 (6) (2014) 588.
[54] Y. Kalachyova, D. Mares, V. Jerabek, P. Ulbrich, L. Lapcak, V. Svorcik, O. Lyutakov, Ultrasensitive and reproducible SERS platform of coupled Ag grating with multibranched Au nanoparticles, Phys. Chem. Chem. Phys. 19 (22) (2017) 14761.
[55] K. Kosuda, J. Bingham, K. Wustholz, R. Van Duyne, Nanostructures and surface-enhanced Raman spectroscopy, in: Handbook of Nanoscale Optics and Electronics, 2010, p. 309.
[56] J. Anastasopoulos, A. Soto Beobide, A. Manikas, G. Voyiatzis, Quantitative surface-enhanced resonance Raman scattering analysis of methylene blue using silver colloid, J. Raman Spectrosc. (2017). http://dx.doi.org/10.1002/jrs.5233. in press.
[57] W. Du, L. Liu, P. Gu, J. Hu, P. Zhan, F. Liu, Z. Wang, Hotspot-engineered quasi-3D metallic network for surface-enhanced Raman scattering based on colloid monolayer templating, Appl. Phys. Lett. 109 (12) (2016) 121108.